Mercury in marine Ordovician/Silurian boundary sections of South China is sulfide-hosted and non-volcanic in origin

Jun Shen [a,b,∗], Thomas J. Algeo [a,c,d], Jiubin Chen [e,f], Noah J. Planavsky [b], Qinglai Feng [a], Jianxin Yu [c], Jinling Liu [g]

[a] *State Key Laboratory of Geological Processes and Mineral Resources, China University of Geosciences, Wuhan, Hubei 430074, PR China*
[b] *Department of Geology and Geophysics, Yale University, New Haven, CT 06520-8109, USA*
[c] *State Key Laboratory of Biogeology and Environmental Geology, China University of Geosciences, Wuhan, Hubei 430074, PR China*
[d] *Department of Geology, University of Cincinnati, Cincinnati, OH 45221-0013, USA*
[e] *Institute of Surface-Earth System Science, Tianjin University, 300072 Tianjin, PR China*
[f] *State Key Laboratory of Environmental Geochemistry (SKLEG), Institute of Geochemistry, Chinese Academy of Science, Guiyang 550081, PR China*
[g] *School of Earth Sciences, China University of Geosciences, Wuhan, Hubei 430074, PR China*

A R T I C L E   I N F O

A B S T R A C T

Mercury (Hg) enrichment in stratigraphic successions is now widely used as a proxy for volcanic inputs, often for the purpose of documenting a relationship between large igneous province (LIP) magmatism and ecosystem perturbations. Earlier studies of Hg in Ordovician/Silurian boundary (OSB) sections in South China and Laurentia identified transient spikes in Hg/TOC ratios, on the basis of which a link between volcanism and the Late Ordovician mass extinction (LOME) was claimed. However, Hg enrichments must be tested based on normalization to their main host phase, and Hg/TOC is a suitable proxy only if Hg is mainly complexed by organic matter in the sediment. Here, we demonstrate that Hg in three OSB sections in South China (Qiliao, Yanzhi, and Jiaoye) is overwhelmingly associated with pyrite, as shown by $r_{(Hg-TS)} > 0.9$ (versus $r_{(Hg-TOC)} < 0.1$) and by EDS elemental mapping. This association requires that Hg concentrations be normalized to pyrite content as proxied by total sulfur [TS], rather than to total organic carbon [TOC]. The resulting Hg/TS profiles show no significant enrichments at any level within the Upper Ordovician–lower Silurian of the study sections. Also, mercury isotope data show constant mass-independent fractionation (Δ^{199}Hg) values ($+0.11 \pm 0.03‰$) that are inconsistent with volcanic inputs. We therefore infer that previous reports of Hg enrichments in OSB sections were due to the presence of Hg-rich sulfides, and that Hg data from both the present and earlier studies provide no evidence of any volcanic influences on the LOME. The results of the present study highlight the need for caution in applying the Hg proxy for volcanic inputs and the importance of evaluating the main host phase of Hg in paleo-marine sediments.

1. Introduction

Massive volcanic eruptions, especially those of large igneous provinces (LIPs), have had a major impact on Earth-surface environments through time, affecting atmospheric composition, climate, ocean chemistry, and the biosphere (Ernst and Youbi, 2017). Although links between LIPs and mass extinctions have been invoked on the basis of carbon-isotope perturbations and coincidences in timing (e.g., Renne et al., 1995), direct geochemical evidence of volcanic inputs to marine sediments during mass ex-

tinction intervals is surprisingly rare, even for large LIPs such as the Siberian Traps and Central Atlantic Magmatic Province (CAMP) (Ernst and Youbi, 2017).

Mercury (Hg) is a relatively new proxy for volcanic inputs to marine sediments. Prior to anthropogenic Hg releases, volcanic fluxes (80–4000 Mg/yr, mean ∼700 Mg/yr) are thought to have accounted for 20–40% of Hg inputs to the Earth-surface environment, and substantially larger fractions during infrequent mega-volcanic eruptions (Pyle and Mather, 2003). Hg is commonly concentrated in volcanic emissions owing to its incompatibility in melts (Canil et al., 2015), with many eruptions emitting sufficient quantities to generate an Hg-enriched event horizon (Schuster et al., 2002). Hg is also present in high concentrations in organic-rich materials (especially coal), and magmatic intrusions of coal fields can lib-
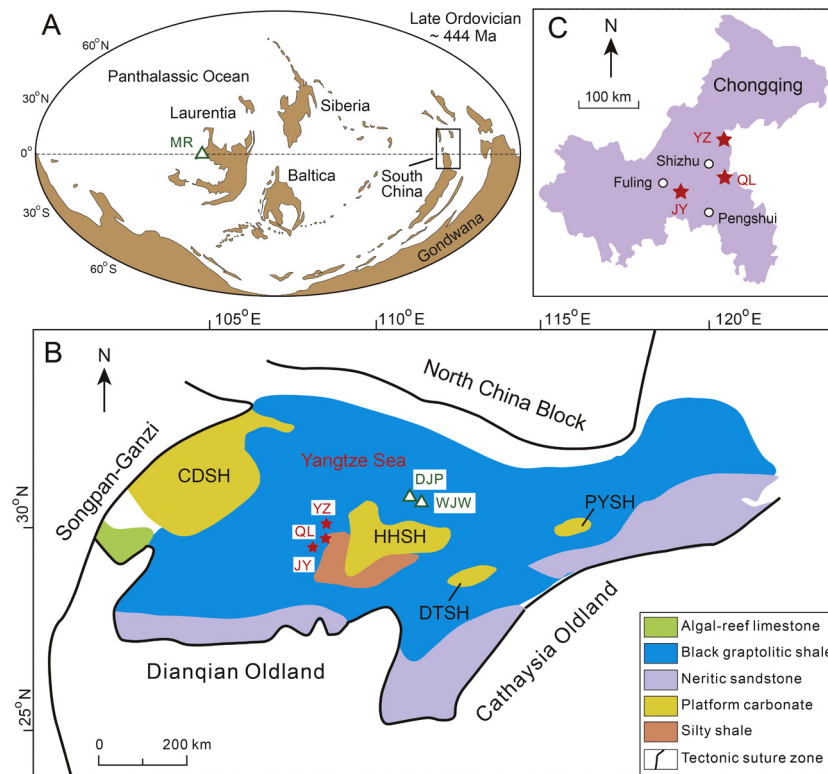
Fig. 1. (A) Global paleogeographic map for Late Ordovician (∼444 Ma) (adapted from Ron Blakey, http://jan.ucc.nau.edu/~rcb7/). (B) Late Ordovician paleogeographic map of the South China Craton (Chen et al., 2004). (C) Locations of study sections. Symbols represent sections analyzed for Hg in this study (red stars) and published sources (green triangles; Gong et al., 2017; Jones et al., 2017). DJP = Dingjiapo; QL = Qiliao section; JY = Jiaoye core; MR = Monitor Range; WJW = Wangjiawan section. YZ = Yanzhi core. DTSH, HHSH, PYSH represent the Dongting, Hunan-Hubei, and Poyang submarine highs respectively. (For interpretation of the colors in the figure(s), the reader is referred to the web version of this article.)

erate large amounts of Hg to the atmosphere (Pyle and Mather, 2003). Large volcanic eruptions can inject Hg-bearing gases into the stratosphere, where Hg has a residence time of ∼0.5–1 yr, allowing long-distance transport and dispersal (Selin, 2009). Mercury washed out of the atmosphere has a sufficiently short residence time in the ocean (∼10^2–10^3 yr) that the signal can be incorporated into marine sediments (Gill and Fitzgerald, 1988). Mercury has a high affinity for organic matter and sulfides and is relatively stable in the burial environment once complexed with these host materials (Ravichandran, 2004).

Mercury mass independent fractionation (MIF) is regarded as a promising tool for tracing Hg sources in ancient depositional systems. MIFs are significant for Hg due to two processes (the nuclear volume and magnetic isotope effects) that are linked to photochemical reactions, i.e., reduction of Hg^{II} or degradation of methyl mercury (Blum et al., 2014). Under oxic conditions, photoreduction of Hg^{II} or methyl mercury to elemental mercury (Hg^0) generally results in small negative MIFs in the products and positive MIFs in the residual reactant (Blum et al., 2014; Yin et al., 2016), whereas photoreduction of Hg^{II} under euxinic conditions yields negative MIFs in the residual reactant (Zheng et al., 2018). The products of photoreduction (e.g., Hg^0) are transported through the atmosphere and eventually removed by absorption and/or wet and dry deposition. In general, marine materials (both sediments and organisms) tend to exhibit positive MIFs and continental materials (including coal, soil, sediments, and plants) negative MIFs. On the other hand, volcanically sourced Hg shows near-zero MIF (+0.02 ± 0.06‰; Yin et al., 2016), which tends to stabilize MIFs in marine sediments during major volcanic events.

The potential of Hg as a volcanic proxy has now been tested for each of the "Big Five" mass extinctions of the Phanerozoic, with mixed results (see reviews in Shen et al., 2019). Partic-

ularly uncertain is whether major volcanic activity was associated with the LOME, which occurred in two stages – one at the start of the Hirnantian glaciation and the other at its termination (Harper et al., 2014). Carbon and sulfur isotopes document a major organic carbon burial event at that time (Zhang et al., 2009), which caused a large decline in atmospheric pCO_2 and global cooling, setting the stage for glaciation (Kump et al., 1999; Finnegan et al., 2011; Algeo et al., 2016). Two studies of Hg in Upper Ordovician sections in South China and Laurentia have documented a few Hg/TOC spikes (Gong et al., 2017; Jones et al., 2017), but the evidence for volcanic influences is tentative and subject to re-interpretation (Fig. 1). One aspect of these studies that needs further investigation is whether TOC-normalization was appropriate; as shown herein, sulfides may be the dominant host of Hg in Ordovician marine units (possibly owing to large-scale sulfide deposition in anoxic oceans of that period; Hammarlund et al., 2012; Zhou et al., 2015), making Hg/TS [note: TS = total sulfur] a superior proxy for evaluating Hg enrichments relative to background levels (Bower et al., 2008).

In this contribution, Hg concentrations as well as Hg isotopes were analyzed for Upper Ordovician–lower Silurian sedimentary strata (dominantly black shales) at three locales in South China. Our goals were to (1) document patterns of Hg enrichment through the Ordovician–Silurian transition (OST), (2) determine the main host phase(s) for Hg in the study units, and (3) evaluate claims for a role of LIP volcanism in the LOME.

2. Geologic background and study sections

During the Ordovician–Silurian transition, the South China Craton was located near the paleo-equator (Fig. 1A). The inner region of the Yangtze Sea was surrounded by the Dianqian Oldland,
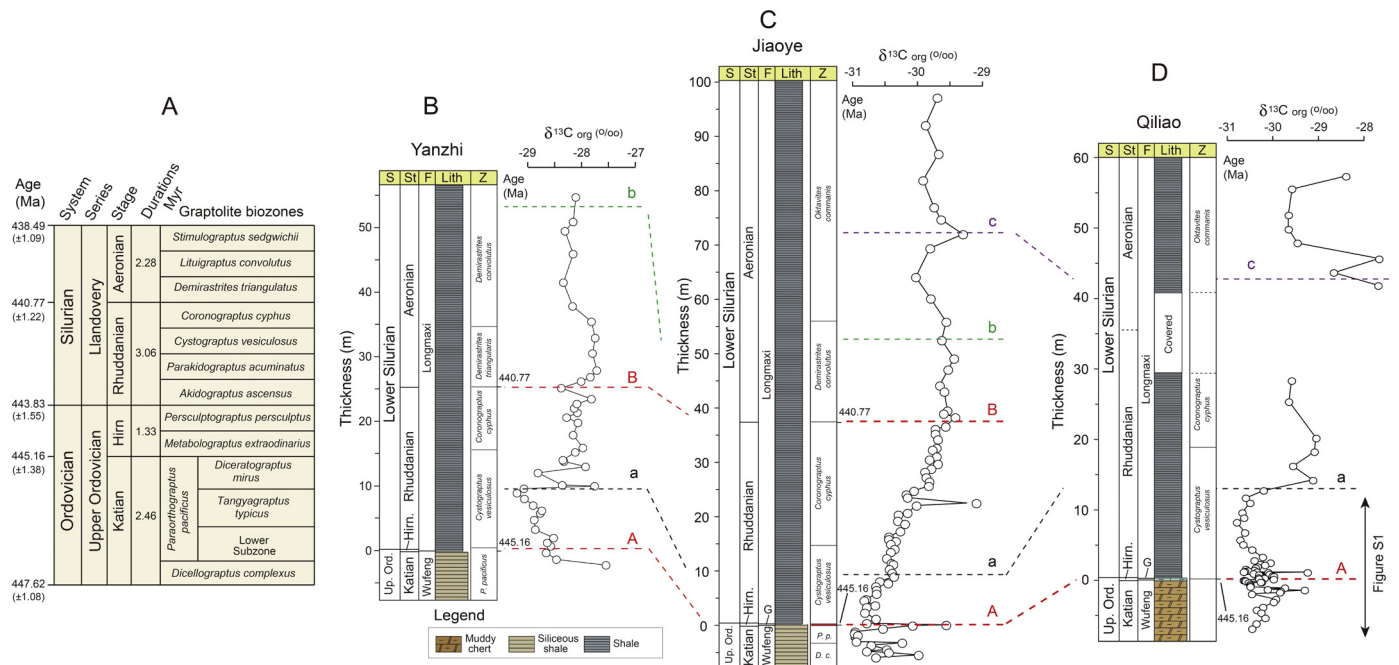
Fig. 2. (A) Age and graptolite zones for the Ordovician–Silurian transition (relatively references see the supplementary materials); (B to D) Correlation of studied successions base on lithology, biostratigraphy and organic carbon isotope. F = Formation, Hirn. = Hirnantian, G = Guanyinqiao Bed, Lith = Lithology, Up. Ord. = Upper Ordovician, S = Series, St = Stage, Z = conodont zone. The red rectangles for Jiaoye represent the two graptolite zones *Metabolographus extraordinarius* and *Persculptograptus persculptus* respectively near the Ordovician/Silurian Boundary. The age (plus/minus in blanket represents the error of the age) of each graptolite zones based on Chen et al. (2015). Note that the Hirnantian Stage straddles the uppermost Wufeng Formation, Guanyinqiao Bed, and lowermost Longmaxi Formation. The higher resolution profile of Qiliao section refer to Fig. S1 in supplementary materials. Refer to the web version for interpretation of color.

Cathaysia Oldland, and Chengdu Submarine High on its northern, eastern, and western margins, respectively (Fig. 1B, Chen et al., 2004) [n.b., modern directions are cited, but note that the South China Craton was rotated ~90° counter-clockwise in the Ordovician]. The inner Yangtze Sea contained several positive topographic features, including the Hunan-Hubei, Dongting, and Poyang submarine highs (Fig. 1B). It accumulated mainly organic-rich black graptolitic shales at water depths of <200 m, although radiolarian cherts are present in some deep-shelf areas of the outer Yangtze Sea (Chen et al., 2004). During the Hirnantian glaciation, shallower sea levels led to widespread deposition of the carbonate-rich Guanyinqiao Bed (Chen et al., 2004).

The study area is located in Chongqing municipality, in an area representing shelf settings of the Upper Yangtze Sea near OSB (Chen et al., 2004). The Qiliao section is an outcrop located in southeastern Shizhu County (29.991°N, 108.105°E), and the Yanzhi (30.115°N, 108.377°E) and Jiaoye (29.613°N, 107.588°E) drillcores are located in southwestern and northeastern Shizhu County, respectively, each being ~100 km distant from the other sites (Fig. 1C). All three sections exhibit a similar lithologic succession through the Ordovician–Silurian transition (Figs. 2, 3). The Wufeng Formation (Katian Stage) consists of ~6 m of siliceous shale at Yanzhi and Jiaoye and ~7 m of muddy cherts at Qiliao (Fig. 3A). The Guanyinqiao Bed (Hirnantian Stage) consists of ~20 cm of argillaceous limestone at Yanzhi and Jiaoye and ~100 cm of argillaceous limestone and mudstone at Qiliao (n.b., for reference purposes, the 0 m level in each section was placed at the base of the Guanyinqiao Bed; Fig. 2). The Longmaxi Formation (uppermost Hirnantian to lower Aeronian stages) consists of 100s of meters of pyritic black shale at all three study locales (Fig. 3B), but only the lowermost 50–100 m of this unit were sampled in the present study. The black shale contains framboidal and rarer euhedral pyrite crystals (Figs. 3D–F) as well as pyritic interbeds of a few centimeters thickness (Fig. 3C) consisting of euhedral pyrite (Figs. 3E, S6). In addition, volcanic ash beds (mm to cm thick,

Fig. 3G) are common throughout the Wufeng and Longmaxi formations at all study locales.

The three study sections are readily intercorrelated on the basis of lithology, biostratigraphy, and chemostratigraphy (e.g., organic carbon isotopes) (Fig. 2). Graptolites are abundant in both the Wufeng and Longmaxi formations (Fig. 3H, I), and graptolite zonation provides a general biostratigraphic framework for South China OSB sections (Chen et al., 2006). The full zonation scheme includes the *Dicellograptus complexus* and *Paraorthograptus pacificus* zones of the Katian Stage, the *Metabolographus extraordinarius* and *Persculptograptus persculptus* zones of the Hirnantian Stage, and the *Cystograptus vesiculosus*, *Coronograptus cyphus*, *Demirastrites triangularis*, *Lituigraptus convolutes*, and *Oktavites communis* zones of the Rhuddanian and early Aeronian stages (Chen et al., 2006). The Yanzhi section spans the *P. pacificus* to *L. convolutus* zones; the Jiaoye section spans the *Di. complexus* to *Li. convolutus* zones; and the Qiliao section spans the *Cy. versiculosus* to *O. communis* zones (Fig. 2). At Qiliao, ~11 m of Lower Silurian strata (at 29–40 m) were not sampled owing to thick soil cover.

Carbon isotope profiles ($\delta^{13}C_{org}$) for the three study sections exhibit similar secular trends (Figs. 2, S1). Upper Ordovician values are relatively light, mostly −29.5 to −28.5‰ at Yanzhi and ~−31 to −30‰ at Jiaoye and Qiliao, with little difference between the Katian and Hirnantian stages. The Qiliao section was sampled at high resolution (~6 cm intervals) around the OSB, allowing it to be correlated in detail with the global stratotype section and point (GSSP) for the Ordovician/Silurian boundary at Wangjiawan (Fig. S1). Similarly low values are observed in the lower *Cy. vesiculosus* Zone (the lowermost Silurian biozone), after which all three sections exhibit rising $\delta^{13}C_{org}$ values through the upper *Cy. vesiculosus* Zone and overlying *Co. cyphus* Zone. This rise was smooth at Jiaoye versus stepwise at Yanzhi, suggesting possible stratigraphic hiatuses in the latter section (n.b., the $\delta^{13}C_{org}$ profile of Qiliao is not sufficiently complete to allow assessment of its pattern). In the overlying *De. triangularis* and *Li. convolutus* zones, $\delta^{13}C_{org}$ values
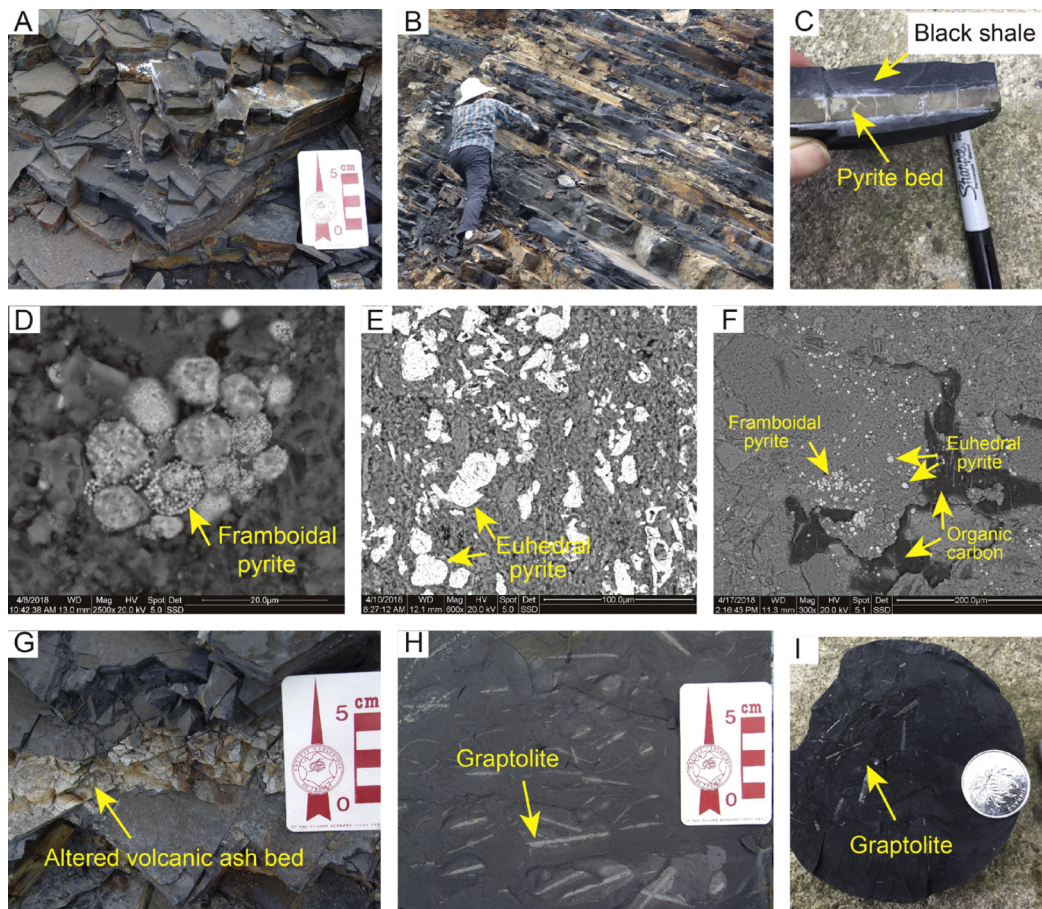
Fig. 3. Field photo of (A) muddy chert from Wufeng Formation (Qiliao); (B) black shale from Longmaxi Formation (Qiliao); (C) pyrite bed (Jiaoye); SEM photo of (D) framboidal pyrites (Jiaoye); (E) euhedral pyrites (Jiaoye); (F) overview of pyrite (both framboidal and euhedral) as well as organic carbon (Jiaoye); (H) altered volcanic ash bed or K-bentonites (Qiliao). Graptolite fossils from outcrop (H) and core (H) (Jiaoye). Refer to the web version for interpretation of the color.

level off at $\sim-28.0\%$ at Yanzhi and $\sim-29.8\%$ at Jiaoye (again, Qiliao cannot be assessed; Fig. 2).

The geochronology of the Ordovician–Silurian transition is well-established based on graptolite stratigraphy and radiometric dating (Figs. 2, S1; Gradstein et al., 2012). The Katian Stage was $\sim2.5 \pm 2.5$ Myr and the Hirnantian–Rhuddanian stages $\sim4.4 \pm 2.6$ Myr in duration; in addition, the lower part of the Aeronian Stage examined in this study corresponds to an interval of $\sim2.0 \pm 2.1$ Myr (Figs. 2, S1). Based on this temporal framework, we constructed an age-depth model for each study section (Fig. S2). Linear sedimentation rates (LSRs) were calculated as stage duration divided by stage thickness. Average LSRs of the Hirnantian–Rhuddanian stages are 5.7 ± 2.2 m/Myr for the Yanzhi core, 8.2 m ± 13.8/Myr for the Jiaoye core, and 5.3 ± 6.6 m/Myr for the Qiliao section (Fig. S2).

3. Methods

Samples were trimmed to remove visible veins and weathered surfaces and pulverized to ~200 mesh in an agate mortar. Aliquots of each sample were prepared for different analytical procedures. A total of 171 black shale samples (70 for Qiliao, 42 for Yanzhi, and 59 for Jiaoye) and 16 pyrite beds (2 for Qiliao, 6 for Yanzhi, and 8 for Jiaoye) were chosen for Hg analysis, and 201 samples (74 for Qiliao, 42 for Yanzhi, and 85 for Jiaoye) for elemental and carbon isotope analyses. Mercury concentrations were analyzed by the Direct Mercury Analyzer (DMA80) at Yale University, as well as Brooks Rand MERX mercury analyzer at School of Earth Sciences, China University of Geosciences (Wuhan). Eleven samples from the

Qiliao section were analyzed in both labs, yielding identical results within error.

A subset of 22 samples from the Qiliao section, including 20 black shale and 2 pyrite beds, were chosen for mercury isotope analysis. Hg isotopes were analyzed on a Nu MC-ICP-MS at the State Key Laboratory of Environmental Geochemistry, Institute of Geochemistry, Chinese Academy of Sciences, Guiyang. We used both major (δ^{202}Hg) and minor (Δ^{199}Hg) mercury isotope data to trace Hg sources in this study (Blum et al., 2014). The results of Hg isotopic measurements are expressed as δ values in units of per mille ($\%$) referenced to the bracketed NIST 3133 Hg standard, as follows: δ^{202}Hg $= [(^{202}$Hg/^{198}Hg$)$ $_{\text{sample}}/(^{202}$Hg/^{198}Hg$)$ $_{\text{standard}} - 1] \times 1000\%$, and Δ^{199}Hg $= \delta^{199}$Hg $- 0.252 \times \delta^{202}$Hg. For more information, see the supplementary material.

Carbon and sulfur were analyzed using a Jena Multi-EA 4000 carbon–sulfur analyzer at the State Key Laboratory of Biogeology and Environmental Geology, China University of Geosciences (Wuhan) (for the Qiliao and Yanzhi samples), and an Eltra 2000 C-S analyzer at the University of Cincinnati (for the Jiaoye and pyrite bed samples). Organic carbon isotopes were analyzed using a MAT-253, and major-element and trace-element concentrations were analyzed using an XRF and ICP-MS, respectively, at the State Key Laboratory of Geological Processes and Mineral Resources, China University of Geosciences (Wuhan). In the same lab, SEM microscopy including EDS elemental spectra were undertaken using an FEI Quanta 200 scanning electron microscope (SEM). Detailed methodological descriptions are given in the supplementary materials.
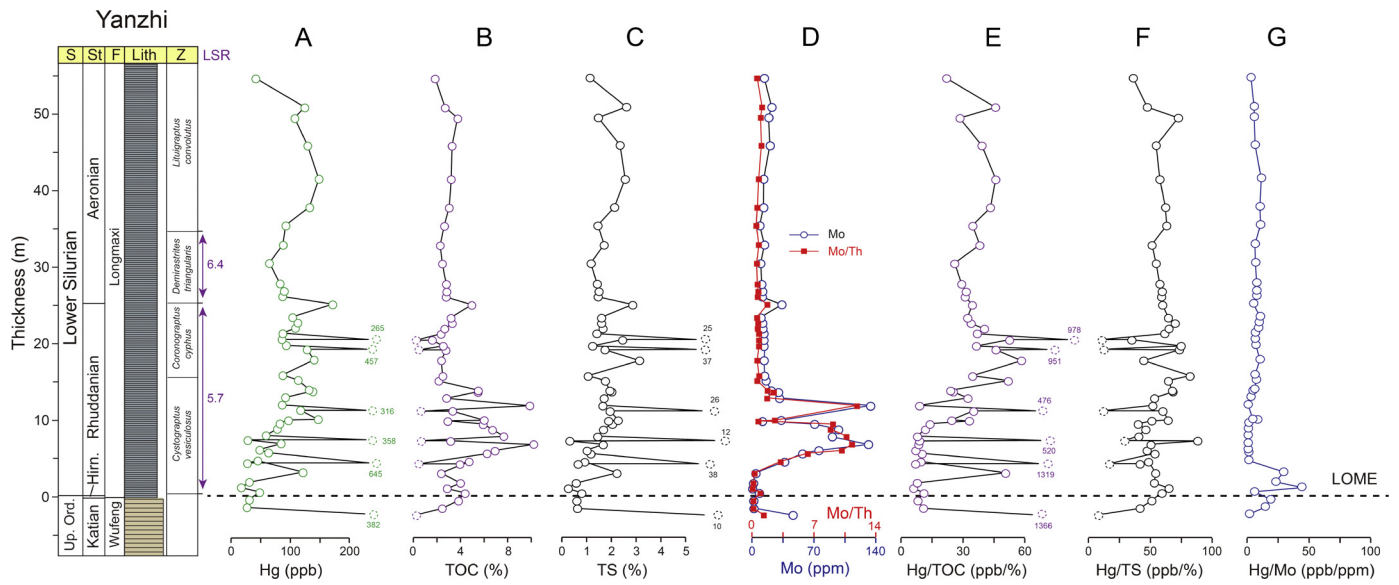
Fig. 4. Yanzhi core profiles of: (A) mercury (Hg) concentration (ppb); (B) total organic carbon (TOC) concentration (%); (C) total sulfur (TS) concentration (%); (D) molybdenum concentration (Mo, ppm) and ratios of molybdenum to thorium (Mo/Th, ppm/ppm); (E) ratios of Hg to TOC (ppb/%); (F) ratios of Hg to total sulfur (Hg/TS, ppb/%); and (G) ratios of Hg to molybdenum (Hg/Mo, ppb/ppm). The dashed open circles represent pyrite samples. The purple numbers represent Linear sedimentation rates (LSR) of each graptolite units. The dashed cycles represent pyrite beds. The horizontal dashed black line represents Latest Ordovician mass extinction (LOME). Other details as in Fig. 2. Refer to the web version for interpretation of the color.
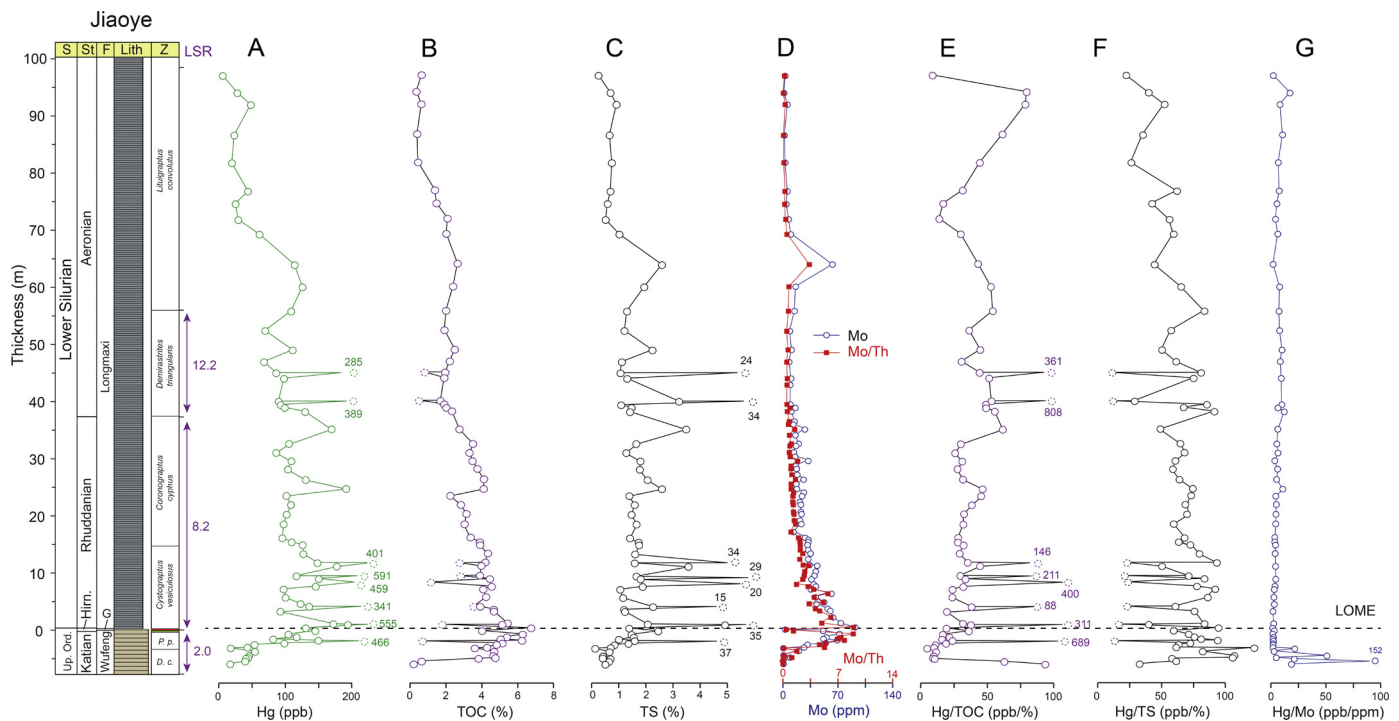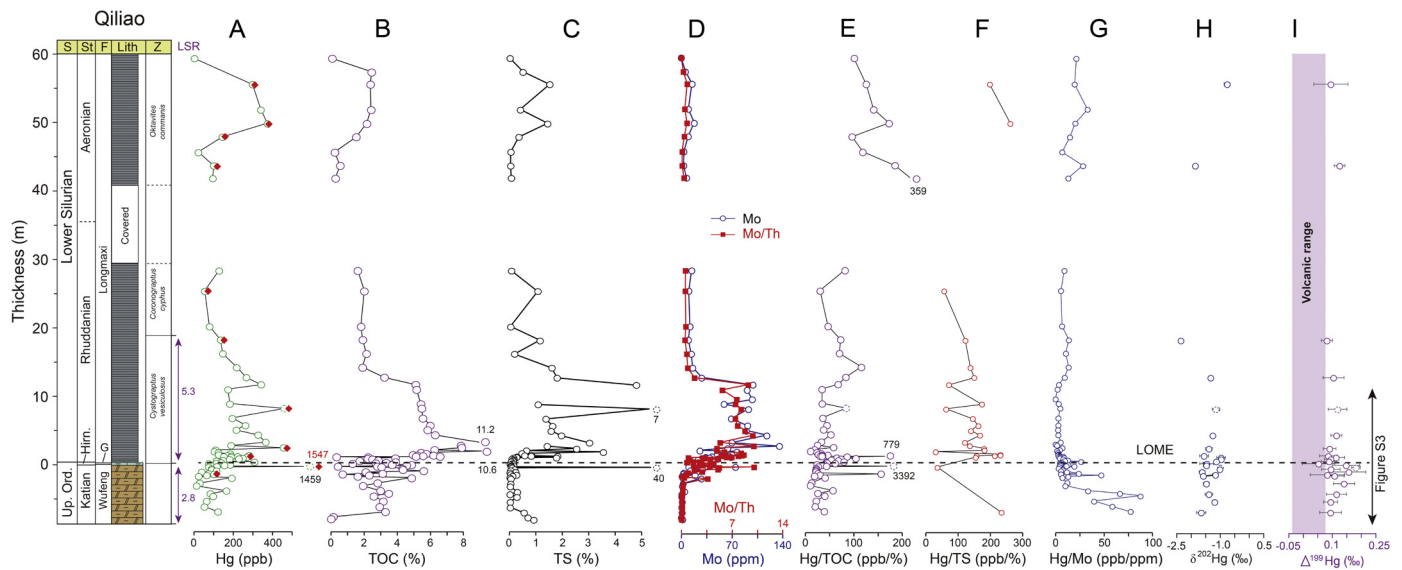

Fig. 5. Jiaoye core profiles of: (A) mercury (Hg) concentration (ppb); (B) total organic carbon (TOC) concentration (%); (C) total sulfur (TS) concentration (%); (D) molybdenum concentration (Mo, ppm) and ratios of molybdenum to thorium (Mo/Th, ppm/ppm); (E) ratios of Hg to TOC (ppb/%); (F) ratios of Hg to total sulfur (Hg/TS, ppb/%); and (G) ratios of Hg to molybdenum (Hg/Mo, ppb/ppm). The purple numbers represent Linear sedimentation rate (LSR) of each graptolite units. The green and red rectangles in graptolite zone represent *Normalograptus extraodinarius*, and *Normalograptus persculptus* respectively. The dashed cycles represent pyrite beds. The horizontal dashed black line represents Latest Ordovician mass extinction (LOME). Note that the Hirnantian Stage straddles the uppermost Wufeng Formation, Guanyinqiao Bed, and lowermost Longmaxi Formation. Other details as in Figs. 2 and 4. Refer to the web version for interpretation of the color.

4. Results

Mercury concentrations are higher at Qiliao (median: 150 ppb, range: 80–279 ppb) than that at Yanzhi (median: 92 ppb, range: 45–148 ppb) and Jiaoye (median: 103 ppb, range: 42–173 ppb) (Figs. 4A, 5A, 6A) [note: all ranges in this study are given as 16th–84th percentiles to avoid influence by outliers]. Despite some variation in absolute concentrations, all three sections show similar stratigraphic patterns. Higher values (>200 ppb for Qiliao and >100 ppb for Yanzhi and Jiaoye, respectively) are observed in the Rhuddanian and lower Aeronian, and lower values (<50 ppb) in the Katian and upper Aeronian. At all three locales, extremely high Hg concentrations (from 265 ppb to 1547 ppb) are present in the pyrite beds as well as in some pyrite-rich black shale samples.

Fig. 6. Qiliao section profiles of: (A) mercury (Hg) concentration (ppb); (B) total organic carbon (TOC) concentration (%); (C) total sulfur (TS) concentration (%); (D) molybdenum concentration (Mo, ppm) and ratios of molybdenum to thorium (Mo/Th, ppm/ppm); (E) ratios of Hg to TOC (ppb/%); (F) ratios of Hg to total sulfur (Hg/TS, ppb/%); and (G) ratios of Hg to molybdenum (Hg/Mo, ppb/ppm); (H) mass-dependent fractionation (δ^{202}Hg,‰); (I) mass-independent fractionation (Δ^{199}Hg,‰). The red diamonds and open circle in column A represent the Hg values measured at Yale University and China University of Geosciences (Wuhan) respectively. The vertical shaded rectangles are the background range values of volcanic Δ^{199}Hg (+0.02 ± 0.06‰; Yin et al., 2016). The Hg/TS profile the samples yielding higher TS values (e.g., >0.5%). The horizontal dashed black line represents Latest Ordovician mass extinction (LOME). Note that the Hirnantian Stage straddles the uppermost Wufeng Formation, Guanyinqiao Bed, and lowermost Longmaxi Formation. Other details as in Figs. 2 and 4. Refer to the web version for interpretation of the color.

TOC contents are similar at Qiliao (median: 3.1%, range: 1.6–5.6%), Yanzhi (median: 2.9%, range: 2.0–5.8%), and Jiaoye (median: 3.3%, range: 1.1–4.7%) (Figs. 4B, 5B, 6B). The TOC profiles show similar trends at all three locales, with higher values (>3.0%) in the lower Rhuddanian and lower values (<3.0%) in the rest of the section. Low TOC values (<2.0%) characterize the pyrite beds.

Total sulfur (TS) is lower at Qiliao (median: 0.25%, range: 0.03–1.6%) than that at Yanzhi (median: 1.7%, range: 0.95–2.8%) and Jiaoye (median: 1.5%, range: 0.69–3.3%) (Figs. 4C, 5C, 6C). The TS profiles show similar trends to the Hg profiles in all three sections. Higher values (>1.5%) are present in the upper Katian to lower Aeronian, and lower values (<1.0%) in the lower Katian and the upper Aeronian. Extremely high TS values (>15%) characterize the pyrite beds.

Both molybdenum concentrations (Mo) and molybdenum/thorium ratios (Mo/Th) exhibit similar secular trends in the three study sections (Figs. 4D, 5D, 6D). Medians (ranges) of Mo values are 20 ppm (3–23 ppm) for Qiliao, 14 ppm (8–59 ppm) for Yanzhi, and 22 ppm (6–51 ppm) for Jiaoye. Medians (ranges) of Mo/Th ratios are 2.7 (0.24–7.7) for Qiliao, 0.76 (0.52–6.6) for Yanzhi, and 1.3 (0.35–4.3) for Jiaoye (note: Mo/Th units are ppm/ppm). The lower Rhuddanian exhibits higher Mo concentrations (>70 ppm at Qiliao and Yanzhi; >40 ppm at Jiaoye) and Mo/Th ratios (>7 at Qiliao and Yanzhi; >4 at Jiaoye) than those in other stratigraphic intervals (where Mo is mostly <20 ppm and Mo/Th <2) (Figs. 4D, 5D, 6D).

Hg/TOC ratios are higher at Qiliao (median: 42, range: 23–103) than that at Yanzhi (median: 33, range: 8.7–52) and Jiaoye (median: 33, range: 17–79; note: Hg/TOC units are ppb/%) (Figs. 4E, 5E, 6E). Hg/TOC profiles are similar in all three sections, with an increasing trend from the Katian (<20 at Yanzhi and Jiaoye, <50 at Qiliao) to the upper Rhuddanian and lower Aeronian (30–100). Extremely high Hg/TOC ratios (>100) characterize the pyrite beds.

Hg/TS ratios exhibit less variation within and between study sections than both raw Hg concentrations and Hg/TOC ratios. Medians (ranges) of Hg/TS ratios for non-pyritic beds are 54 (38–67) at Yanzhi, 63 (31–83) at Jiaoye, and 155 (88–217) at Qiliao (note:

Hg/TS units are ppb/%) (Figs. 4F, 5F, 6F). Pyrite-rich shale samples and pyrite beds show significantly lower Hg/TS ratios (<20).

Hg/Mo ratios are similar at Qiliao (median: 7.0, range: 3.0–23), Yanzhi (median: 6.5, range: 1.2–11), and Jiaoye (median: 4.7, range: 2.0–10; note: Hg/Mo units are ppb/ppm) (Figs. 4G, 5G, 6G). Variation in Hg/Mo ratios is limited, except for a few peaks (to 50–100) in the Katian Stage at Jiaoye (Fig. 5G) and Qiliao (Fig. 6G), and in the basal Rhuddanian at Yanzhi (Fig. 4G). Hg/Mo ratios are similar in the black shale samples and pyrite beds.

Major mercury isotopes (δ^{202}Hg) are relatively uniform for all samples, with values ranging from −1.5‰ to −1.0 ‰, yielding an average of −1.36 ± 0.35‰ ($n = 22$) (Fig. 6H). Minor mercury isotopes (Δ^{199}Hg) are also relatively uniform, with values averaging +0.11 ± 0.03 ‰ ($n = 22$) (Fig. 6I). Mercury isotope values do not show any apparent relationship to lithology, being similar for muddy cherts, black shales, and pyrite beds (Fig. 6H, 6I).

5. Discussion

5.1. Host phases of mercury in marine sediments

Mercury can reside in several sediment fractions, including organic matter, clay minerals, sulfides, and other phases (Ravichandran, 2004; Selin, 2009). Organic matter is generally the most important host of Hg in modern and many ancient marine sediments, mainly in the form of organic–Hg complexes (Ravichandran, 2004). Clay minerals can also adsorb Hg^{II} owing to their high surface area and surface charges (Farrah and Pickering, 1978), leading to significant terrestrial Hg contributions to shallow-marine sediments (Them et al., 2019). Sulfide minerals can be the main host for Hg in euxinic facies owing to the high affinity of Hg for sulfide (Bower et al., 2008; Han et al., 2014; Duan et al., 2016). In such facies, aqueous Hg^{II} can be removed to the sediment by formation of HgS as well as adsorption onto iron sulfides (Benoit et al., 1999; Bouffard and Amyot, 2009). Sulfide minerals such as pyrite (FeS$_2$), pyrrhotite (Fe$_{1-x}$S), and mackinawite (FeS) have been demonstrated to host large amounts of Hg in some natural settings (Wolfenden et al., 2005; Han et al., 2014;
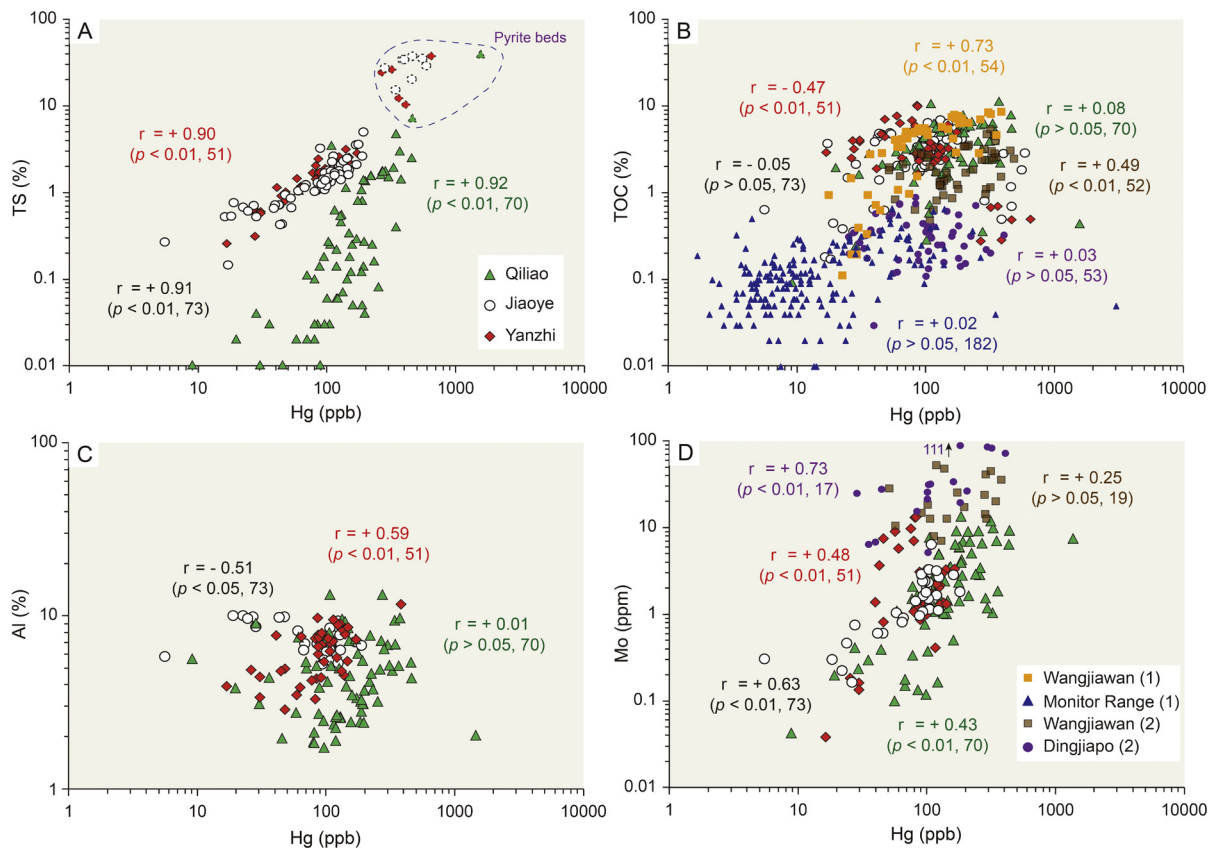
Fig. 7. Crossplots of: (A) TS and Hg; (B) TOC and Hg; (C) Al and Hg; and (D) Mo and Hg. The data source for Wangjiawan (1) and Monitor Range (1) from Jones et al. (2017); the data source of Wangjiawan (2) and Dingjiaping (2) from Gong et al. (2017). r represents the positive ($+$), and negative ($-$) correlation coefficient. The number in the bracket (behind comma) represent the number of samples. Refer to the web version for interpretation of the color.

Dziok et al., 2018) as well as in laboratory experiments (Duan et al., 2016). Uptake of Hg by sulfides is facilitated by the high stability constants of inorganic Hg–S complexes (ranging from 10^{23} to 10^{38}), exceeding those of organic–Hg complexes (10^{22} to 10^{28}) (Ravichandran, 2004). Because Hg^{II} and S^{2-} represent a soft Lewis acid and a soft Lewis base, respectively, they have a strong chemical affinity and bond readily (Ravichandran, 2004). This can lead to formation of solid-phase HgS in sediments, which is relatively insoluble and less volatile than other forms of sedimentary Hg (Wolfenden et al., 2005).

In the present study, several lines of evidence indicate that Hg is hosted primarily by sulfides, with lesser amounts associated with the organic and clay-mineral fractions. First, Hg exhibits much higher correlation coefficients with TS ($r = +0.92$, $+0.90$, $+0.91$ for Qiliao, Yanzhi, and Jiaoye, respectively; $n = 51$–73; $p < 0.01$) than with TOC ($r = +0.08$, -0.47, and -0.05; $p > 0.05$, >0.01, and >0.05) or with Al ($r = +0.01$, $+0.59$, and -0.51; $p > 0.05$, >0.01, and >0.01) (Fig. 7A–C). Second, there is a strong association between higher Hg concentrations and sulfide content (as shown by both the pyrite-rich black shales and the pyrite beds; Figs. 4–6). Third, EDS elemental mapping demonstrates conclusively that Hg is hosted mainly in pyrite crystals (both framboidal and euhedral), with little if any present in the organic and clay-mineral fractions (Figs. 8, 9). The relatively high Hg concentrations and Hg–TS correlation coefficients of the Qiliao section suggest that, despite somewhat lower TS content, sulfide is still the main sedimentary host phase for Hg (Fig. 7).

Normalization of Hg concentrations to TOC is not appropriate in cases where organic matter is not the main host phase. The host phase of Hg in earlier studies of the OSB (Gong et al., 2017; Jones et al., 2017) was not determined and cannot be tested

retroactively because of a lack of sulfur concentration data in those reports. We note, however, that the correlations between Hg and TOC are insignificant ($p > 0.05$) for both Dingjiapo, South China ($r = +0.03$, $n = 53$) and Monitor Range, Nevada ($r = +0.02$, $n = 182$; Fig. 7B), suggesting that the organic fraction was not the main host of Hg in those sections (note: a third section at Wangjiawan shows a significant Hg–TOC correlation in both Gong et al. (2017), and Jones et al. (2017), with $r = +0.49$ and $+0.73$, $n = 52$ and 54, respectively; $p < 0.01$). On the other hand, samples from Dingjiapo show a high correlation between Hg and Mo (Fig. 7D, $r = +0.73$, $p < 0.01$, $n = 17$), which is consistent with a redox control. If Hg is mainly hosted by the sulfide fraction, as shown in the present study, then it is more appropriate to normalize Hg concentrations to total sulfur (TS). Unlike Gong et al. (2017) and Jones et al. (2017), who inferred significant Hg/TOC peaks during the Hirnantian Stage, our results based on Hg/TS ratios show no peaks within this interval (Figs. 4–6), even in the high-resolution Qiliao section (Fig. S3).

5.2. Environmental controls on mercury uptake by marine sediments

In modern aqueous systems, Hg can be affected by a number of environmental factors during transfer from the water column to the sediment, among which redox conditions and sedimentation rates are most important (Ravichandran, 2004). Reducing conditions promote organic matter preservation and formation of Hg–OM complexes, which are commonly the dominant form of Hg in marine sediments, as well as links between Hg and thiol functional groups (Ravichandran, 2004). Furthermore, the transformation from Hg to particle-reactive methyl-Hg is facilitated by sulfate reduction (Gilmour et al., 1992) and certain forms of organic
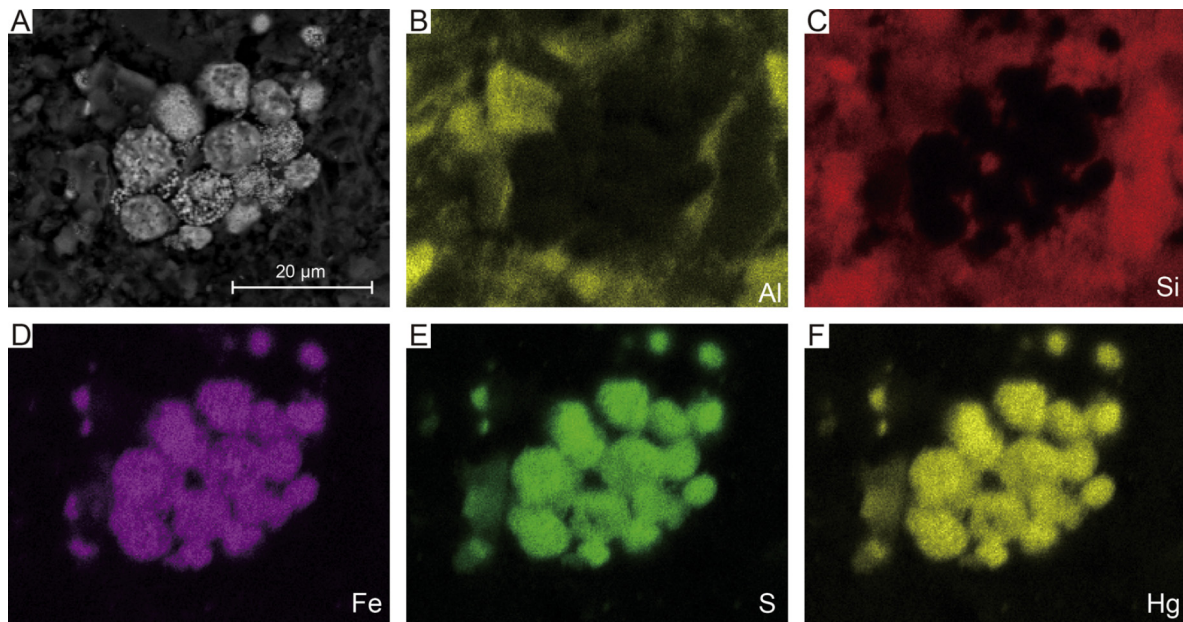
Fig. 8. Elemental map of framboidal pyrites (original picture refers to Fig. 3D). (A) SEM photo; (B) Aluminum (Al); (C) Silicon (Si); (D) iron (Fe); (E) Sulfur (S); (F) mercury (Hg). Refer to the web version for interpretation of the color.
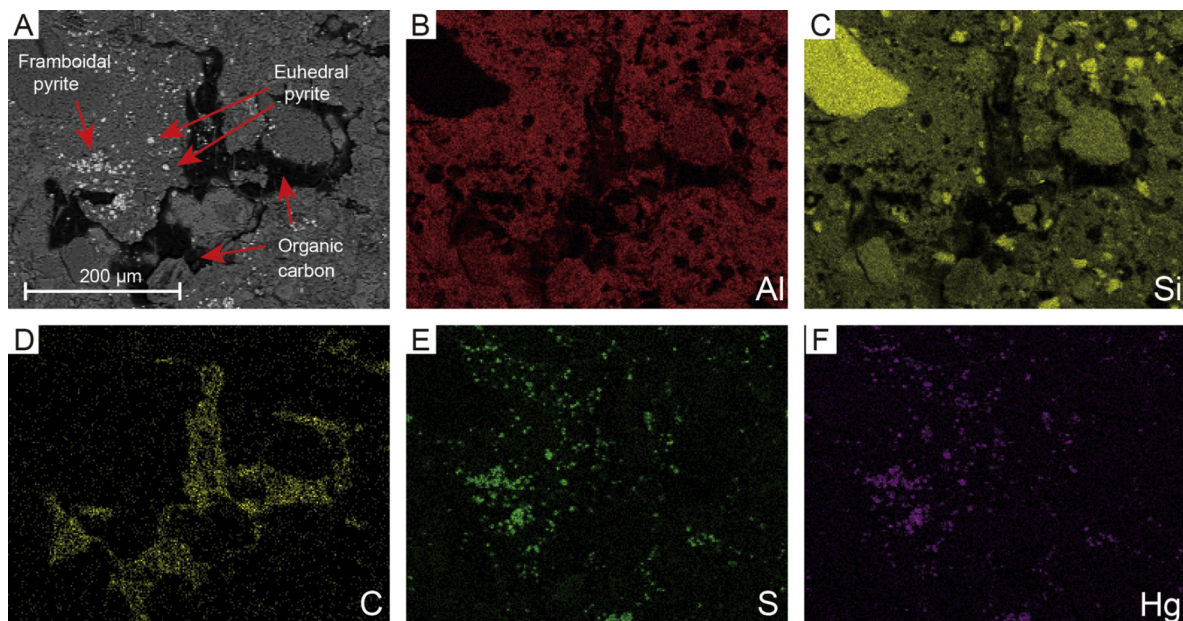
Fig. 9. Elemental map of framboidal pyrites, euhedral pyrites as well as organic carbon (original picture refers to Fig. 3F). (A) SEM photo; (B) aluminum (Al); (C) silicon (Si); (D) carbon (C); (E) sulfur (S); (F) mercury (Hg). Refer to the web version for interpretation of the color.

matter (Zhu et al., 2018). Reducing conditions also favor formation of HgS and uptake of Hg by iron sulfides (Bower et al., 2008; Duan et al., 2016). In the present study, redox conditions are likely to have been the main control on removal of Hg to the sediment. Hg and Mo concentrations are significantly correlated at Yanzhi ($r = +0.48$, $n = 51$), Jiaoye ($r = +0.63$, $n = 73$), and Qiliao ($r = +0.43$, $n = 70$; $p < 0.01$ at all sites; Fig. 7D), reflecting Mo uptake under intensely reducing conditions (Algeo and Lyons, 2006). Furthermore, it is unlikely that Hg was taken up by pyrite after release from remineralized sedimentary organic matter because the bulk of the pyrite in this study consists of small framboids (<5 μm diam., Fig. 8A) that probably formed in the water column.

Higher sedimentation rates tend to dilute the main sediment components (i.e., organic matter, sulfides) that host Hg, which reduces the Hg concentration of sediments but does not affect Hg burial fluxes (Gobeil et al., 1999). However, sedimentation rates appear to have played an insignificant role in Hg uptake by the study samples. Despite variations in LSRs from 8.2 to 12.2 m/Myr in the lower Longmaxi Formation at Jiaoye (Fig. 5), Hg contents remained stable and high (Fig. 2). Furthermore, Hg contents and LSRs exhibit no significant correlations in the three study sections ($r = +0.12$, $n = 7$; $p > 0.05$) (Fig. S4). Although detrital Hg inputs can be significant in some marine systems (e.g., Toarcian Oceanic Anoxic Event; Them et al., 2019), terrestrial Hg sources are not regarded as having been significant in the present study units owing to weak correlations between Hg and Al (Fig. 7D; see above).

5.3. Evaluation of volcanic Hg inputs during the Ordovician–Silurian transition

Euxinic facies can become Hg-enriched through uptake from normal seawater, without any external (e.g., volcanic) Hg sources. For example, Hg concentrations range from 314 to 488 ppb in Pleistocene Mediterranean sapropels (Gehrke et al., 2009) and from 200 to 600 ppb in many ancient black shales (Ketris and Yudovich, 2009). In this context, the average Hg concentrations of the Wufeng–Longmaxi black shales (excluding the pyrite beds) at Qiliao (170 ± 100 ppb), Jiaoye (90 ± 46 ppb), and Yanzhi (95 ± 57 ppb) are not exceptional and may have been derived from seawater without volcanic inputs. Although Hg/TS has not been reported in most studies of ancient marine sediments undertaken to date, the Hg/TS ratios of the present study sections (53–150 ppb/%) are similar to those in coals (190–440 ppb/%), where Hg is commonly hosted by sulfides (Dziok et al., 2018), and in experimentally precipitated sulfides (to 10^4–10^5 ppb/%) (Bower et al., 2008; Duan et al., 2016).

Minor mercury isotopes (Δ^{199}Hg) that display MIF have used as a tracer for Hg sources in marine sediments (Blum et al., 2014). Mercury from volcanic sources exhibits near-zero Δ^{199}Hg with limited variation (+0.02 ± 0.06‰) Yin et al., 2016), whereas photoreduction of aqueous Hg^{II} yields positive MIF values in normal marine sediments (Gehrke et al., 2009; Blum et al., 2014), although photoreduction of sulfur ligands under sulfide-rich conditions can yield slightly negative MIF values (Zheng et al., 2018). MIF has been used to explore volcanic Hg inputs during major biocrises at the Permian–Triassic (Grasby et al., 2017) and Triassic–Jurassic boundaries (Thibodeau et al., 2016), and values close to zero have been interpreted as evidence of volcanic Hg inputs that did not undergo photoreduction during transport (Chen et al., 2012). In the Qiliao section, MIF ranges from +0.05‰ to +0.15‰, which is within the range for normal marine sediments (Gehrke et al., 2009; Blum et al., 2014) and slight higher than that for volcanic Hg (Yin et al., 2016), providing no evidence of volcanic influence. Furthermore, MIF values at Qiliao are nearly uniform through the Upper Ordovician and lower Silurian (an ~8-Myr interval, Fig. 6), and the absence of any significant changes argues against volcanic Hg sources. Also, δ^{202}Hg values (−2.5‰ to −1.0‰) are similar to those of normal marine sediments, although δ^{202}Hg is subject to multiple mass-dependent influences related to physical, chemical and biological processes (Blum et al., 2014). Our results are similar to those reported by Gong et al. (2017) (Δ^{199}Hg = +0.05‰ to +0.20‰; δ^{202}Hg = −2.0‰ to −0.5‰), indicating similar Hg cycling processes across South China during the O–S transition.

Because Hg has a strong affinity for pyrite (Bower et al., 2008; Duan et al., 2016), it is not necessary to invoke external (i.e., volcanic) inputs to account for Hg enrichment in pyrite-rich units. The Wufeng and Longmaxi black shales contain numerous pyrite beds, and these beds show only modest Hg enrichments (Hg/TS ratios <300 ppb/%), providing no evidence for external Hg inputs. Furthermore, the pyrite beds yield major and minor mercury isotope values similar to those of the enclosing black shales, implying a common Hg source (i.e., seawater). Although the concentration of Hg in OSB seawater is unknown, the high stability constants of inorganic Hg–S complexes (Ravichandran, 2004; Bower et al., 2008) may have facilitated large-scale Hg uptake by pyrite in strongly anoxic OSB oceans.

The study area was subject to sporadic volcanic activity from the Late Ordovician (Katian) to the Early Silurian (Aeronian), and numerous volcanic ash beds were deposited in the Wufeng and Longmaxi formations (Su et al., 2009). However, these eruptions did not play a significant role in the LOME because volcanic ash is found throughout a thick stratigraphic interval (e.g., >6 m in the Wangjiawan GSSP, from the lower Katian to the lower Rhuddanian)

and is not concentrated around the extinction horizons or within the Hirnantian Stage (Su et al., 2009). Furthermore, Hg/TS ratios do not increase near the extinction horizons, and Hg isotope data do not show a volcanic signature (see above). Therefore, earlier claims of a linkage between volcanism, Hg/TOC enrichments, and the LOME (e.g., Gong et al., 2017; Jones et al., 2017) need to be critically re-evaluated.

5.4. No evidence for an end-Ordovician large igneous province

Several studies have claimed that a LIP eruption was the cause of the end-Ordovician mass extinction, based on little to no supporting evidence (e.g., Lefebvre et al., 2010; Ernst and Youbi, 2017). Frequently, this claim has been made in the context of discussing the known relationships of the Permian–Triassic boundary (PTB) and Triassic–Jurassic boundary (TJB) mass extinctions to the Siberian Traps (Reichow et al., 2009) and CAMP large igneous provinces (Marzoli et al., 2004), respectively, and the possible relationship of the Cretaceous–Paleogene boundary (KPB) mass extinction to the Deccan Traps (Schoene et al., 2015). In the view of some LIP researchers, these well-established examples "prove" that all of the Big Five mass extinctions (including the end-Ordovician and late Devonian ones) can be related to the same mechanism (i.e., LIP magmatism). However, the end-Ordovician and late Devonian mass extinctions are quite different in character from the PTB, TJB and KPB extinctions, being more protracted in duration, associated with long-term cooling rather than warming, and lacking any association to a known major LIP (Algeo et al., 1995, 2016). These features suggest primary causes linked to massive organic carbon burial, triggered by bioevolutionary mechanisms (e.g., appearance of vascular land plants) rather than endogenic causes (Algeo et al., 1995; Lenton et al., 2012). The results of the present study provide no support for LIP volcanism during the O–S transition.

6. Conclusions

Analysis of the mercury concentrations and isotopic compositions of black shales and pyrite beds in three Ordovician/Silurian boundary successions in South China (Qiliao, Yanzhi, and Jiaoye) formed the basis for a re-evaluation of the role of volcanism in the Late Ordovician Mass Extinction (LOME). Our results demonstrate that the sulfide fraction (i.e., pyrite) instead of the organic fraction is the dominant host of Hg in the Wufeng and Longmaxi formations, as shown by $r_{(Hg–TS)}$ >0.9 (versus $r_{(Hg–TOC)}$ < 0.1) and by spatial correspondence of Hg and S as revealed through EDS elemental mapping. When normalized to total sulfur content, our data reveal no significant spikes in Hg enrichment within the study sections. Mercury isotope data from a subset of samples show constant mass-independent fractionation (Δ^{199}Hg) values (+0.11 ± 0.03‰) that are inconsistent with volcanic inputs. We therefore infer that previous reports of Hg enrichments in OSB sections were due to an abundance of sulfides, and that the existing Hg data (from both the present and earlier studies) provide no evidence of any volcanic influence on the LOME. The results of the present study highlight the need for caution in applying the Hg proxy for volcanic inputs and the importance of evaluating the main host phase of Hg in marine sediments.

Acknowledgements

Appendix A. Supplementary material

Supplementary material related to this article can be found online at https://doi.org/10.1016/j.epsl.2019.01.028.

References

Algeo, T.J., Lyons, T.W., 2006. Mo-total organic carbon covariation in modern anoxic marine environments: implications for analysis of paleoredox and paleohydrographic conditions. Paleoceanography 21 (1), PA1016, 25 pp.

Algeo, T.J., Berner, R.A., Maynard, J.B., Scheckler, S.E., 1995. Late Devonian oceanic anoxic events and biotic crises: "rooted" in the evolution of vascular land plants. GSA Today 5 (3), 64–66, 45.

Algeo, T.J., Marenco, P.J., Saltzman, M.R., 2016. Co-evolution of oceans, climate, and the biosphere during the 'Ordovician Revolution': a review. Palaeogeogr. Palaeoclimatol. Palaeoecol. 458, 1–11.

Benoit, J.M., Gilmour, C.C., Mason, R.P., Heyes, A., 1999. Sulfide controls on mercury speciation and bioavailability to methylating bacteria in sediment pore waters. Environ. Sci. Technol. 33, 951–957.

Blum, J.D., Sherman, L.S., Johnson, M.W., 2014. Mercury isotopes in earth and environmental sciences. Annu. Rev. Earth Planet. Sci. 42, 249–269.

Bouffard, A., Amyot, M., 2009. Importance of elemental mercury in lake sediments. Chemosphere 74, 1098–1103.

Bower, J., Savage, K.S., Weinman, B., Barnett, M.O., Hamilton, W.P., Harper, W.F., 2008. Immobilization of mercury by pyrite (FeS$_2$). Environ. Pollut. 156, 504–514.

Canil, D., Crockford, P.W., Rossin, R., Telmer, K., 2015. Mercury in some arc crustal rocks and mantle peridotites and relevance to the moderately volatile element budget of the Earth. Chem. Geol. 396, 134–142.

Chen, J., Hintelmann, H., Feng, X., Dimock, B., 2012. Unusual fractionation of both odd and even mercury isotopes in precipitation from Peterborough, ON, Canada. Geochim. Cosmochim. Acta 90, 33–46.

Chen, X., Rong, J., Li, Y., Boucot, A.J., 2004. Facies patterns and geography of the Yangtze region, South China, through the Ordovician and Silurian transition. Palaeogeogr. Palaeoclimatol. Palaeoecol. 204, 353–372.

Chen, X., Rong, J., Fan, J., Zhan, R., Mitchell, C.E., Harper, D.A., Melchin, M.J., Peng, P.A., Finney, S.C., Wang, X., 2006. The Global Boundary Stratotype Section and Point (GSSP) for the base of the Hirnantian Stage (the uppermost of the Ordovician System). Episodes 29, 183–196.

Chen, X., Fan, J.X., Zhang, Y.D., Wang, H.Y., Chen, Q., Wang, W.H., Liang, F., Guo, W., Zhao, Q., Nie, H.K., Wen, Z.D., Sun, Z.Y., 2015. Subdivision and delineation of the Wufeng and Longmaxi black shales in the subsurface areas of the Yangtze platform. J. Stratigr. 39, 351–358 (in Chinese with English abstract).

Cooper, R.A., Sadler, P.M., 2012. The Ordovician period. In: Gradstein, F.M., Ogg, J.G., Schmitz, M.A., Ogg, G. (Eds.), The Geologic Time Scale 2012. Elsevier, Amsterdam, pp. 489–523.

Duan, Y., Han, D.S., Batchelor, B., Abdel-Wahab, A., 2016. Synthesis, characterization, and application of pyrite for removal of mercury. Colloids Surf. A, Physicochem. Eng. Asp. 490, 326–335.

Dziok, T., Strugała, A., Włodek, A., 2018. Studies on mercury occurrence in inorganic constituents of Polish coking coals. Environ. Sci. Pollut. Res. 12 pp. https://doi.org/10.1007/s11356-018-1667-1.

Ernst, R.E., Youbi, N., 2017. How Large Igneous Provinces affect global climate, sometimes cause mass extinctions, and represent natural markers in the geological record. Palaeogeogr. Palaeoclimatol. Palaeoecol. 478, 30–52.

Fan, J.X., Peng, P.A., Melchin, M., 2009. Carbon isotopes and event stratigraphy near the Ordovician–Silurian boundary, Yichang, South China. Palaeogeogr. Palaeoclimatol. Palaeoecol. 276, 160–169.

Farrah, H., Pickering, W.F., 1978. The sorption of mercury species by clay minerals. Water Air Soil Pollut. 9, 23–31.

Finnegan, S., Bergmann, K., Eiler, J.M., Jones, D.S., Fike, D.A., Eisenman, I., Hughes, N.C., Tripati, A.K., Fischer, W.W., 2011. The magnitude and duration of Late Ordovician–Early Silurian glaciation. Science 331, 903–906.

Gehrke, G.E., Blum, J.D., Meyers, P.A., 2009. The geochemical behavior and isotopic composition of Hg in a mid-Pleistocene western Mediterranean sapropel. Geochim. Cosmochim. Acta 73, 1651–1665.

Gill, G.A., Fitzgerald, W.F., 1988. Vertical mercury distributions in the oceans. Geochim. Cosmochim. Acta 52, 1719–1728.

Gilmour, C.C., Henry, E.A., Mitchell, R., 1992. Sulfate stimulation of mercury methylation in freshwater sediments. Environ. Sci. Technol. 26, 2281–2287.

Gobeil, C., Macdonald, R.W., Smith, J.N., 1999. Mercury profiles in sediments of the Arctic Ocean basins. Environ. Sci. Technol. 33, 4194–4198.

Gong, Q., Wang, X., Zhao, L., Grasby, S.E., Chen, Z.-Q., Zhang, L., Li, Y., Cao, L., Li, Z., 2017. Mercury spikes suggest volcanic driver of the Ordovician–Silurian mass extinction. Sci. Rep. 7, 5304. https://doi.org/10.1038/s41598-017-05524-5.

Gradstein, F.M., Ogg, J.G., Schmitz, M.A., Ogg, G. (Eds.), 2012. The Geologic Time Scale, Vol. 2. Elsevier, Amsterdam.

Grasby, S.E., Shen, W., Yin, R., Gleason, J.D., Blum, J.D., Lepak, R.F., Hurley, J.P., Beauchamp, B., 2017. Isotopic signatures of mercury contamination in latest Permian oceans. Geology 45, 55–58.

Hammarlund, E.U., Dahl, T.W., Harper, D.A., Bond, D.P., Nielsen, A.T., Bjerrum, C.J., Schovsbo, N.H., Schönlaub, H.P., Zalasiewicz, J.A., Canfield, D.E., 2012. A sulfidic driver for the end-Ordovician mass extinction. Earth Planet. Sci. Lett. 331, 128–139.

Han, D.S., Orillano, M., Khodary, A., Duan, Y., Batchelor, B., Abdel-Wahab, A., 2014. Reactive iron sulfide (FeS)-supported ultrafiltration for removal of mercury (Hg (II)) from water. Water Res. 53, 310–321.

Harper, D.A., Hammarlund, E.U., Rasmussen, C.M., 2014. End Ordovician extinctions: a coincidence of causes. Gondwana Res. 25, 1294–1307.

Jones, D.S., Martini, A.M., Fike, D.A., Kaiho, K., 2017. A volcanic trigger for the Late Ordovician mass extinction? Mercury data from south China and Laurentia. Geology 45, 631–634.

Ketris, M., Yudovich, Y.E., 2009. Estimations of Clarkes for Carbonaceous biolithes: world averages for trace element contents in black shales and coals. Int. J. Coal Geol. 78, 135–148.

Kump, L., Arthur, M., Patzkowsky, M., Gibbs, M., Pinkus, D., Sheehan, P., 1999. A weathering hypothesis for glaciation at high atmospheric pCO$_2$ during the Late Ordovician. Palaeogeogr. Palaeoclimatol. Palaeoecol. 152, 173–187.

Lefebvre, V., Servais, T., François, L., Averbuch, O., 2010. Did a Katian large igneous province trigger the Late Ordovician glaciation? A hypothesis tested with a carbon cycle model. Palaeogeogr. Palaeoclimatol. Palaeoecol. 296 (3–4), 310–319.

Lenton, T.M., Crouch, M., Johnson, M., Pires, N., Dolan, L., 2012. First plants cooled the Ordovician. Nat. Geosci. 5 (2), 86–89.

Marzoli, A., Bertrand, H., Knight, K.B., Cirilli, S., Buratti, N., Vérati, C., Nomade, S., Renne, P.R., Youbi, N., Martini, R., Allenbach, K., 2004. Synchrony of the Central Atlantic magmatic province and the Triassic–Jurassic boundary climatic and biotic crisis. Geology 32 (11), 973–976.

Melchin, M.J., Sadler, P.M., Cramer, B.D., 2012. In: Gradstein, F.M., Ogg, J.G., Schmitz, M.A., Ogg, G. (Eds.), The Geologic Time Scale 2012. Elsevier, Amsterdam, pp. 525–558.

Pyle, D.M., Mather, T.A., 2003. The importance of volcanic emissions for the global atmospheric mercury cycle. Atmos. Environ. 37, 5115–5124.

Ravichandran, M., 2004. Interactions between mercury and dissolved organic matter—a review. Chemosphere 55, 319–331.

Reichow, M.K., Pringle, M.S., Al'Mukhamedov, A.I., Allen, M.B., Andreichev, V.L., Buslov, M.M., Davies, C.E., Fedoseev, G.S., Fitton, J.G., Inger, S., Medvedev, A.Y., Saunders, A.D., 2009. The timing and extent of the eruption of the Siberian Traps large igneous province: implications for the end-Permian environmental crisis. Earth Planet. Sci. Lett. 277 (1–2), 9–20.

Renne, P.R., Black, M.T., Zichao, Z., Richards, M.A., Basu, A.R., 1995. Synchrony and causal relations between Permian–Triassic boundary crises and Siberian flood volcanism. Science 269 (5229), 1413–1416.

Schoene, B., Samperton, K.M., Eddy, M.P., Keller, G., Adatte, T., Bowring, S.A., Khadri, S.F., Gertsch, B., 2015. U–Pb geochronology of the Deccan Traps and relation to the end-Cretaceous mass extinction. Science 347 (6218), 182–184.

Schuster, P.F., Krabbenhoft, D.P., Naftz, D.L., Cecil, L.D., Olson, M.L., Dewild, J.F., Susong, D.D., Green, J.R., Abbott, M.L., 2002. Atmospheric mercury deposition during the last 270 years: a glacial ice core record of natural and anthropogenic sources. Environ. Sci. Technol. 36 (11), 2303–2310.

Selin, N.E., 2009. Global biogeochemical cycling of mercury: a review. Ann. Rev. Environ. Resour. 34, 43–63.

Shen, J., Algeo, T.J., Planavsky, N.J., Yu, J.X., Feng, Q.L., Song, H.J., Song, H.Y., Rowe, H., Zhou, L., Chen, J.B., 2019. Mercury enrichments provide evidence of Early Triassic volcanism following the end-Permian mass extinction. Earth-Sci. Rev. In press.

Su, W., Huff, W.D., Ettensohn, F.R., Liu, X., Zhang, J.E., Li, Z., 2009. K-bentonite, black-shale and flysch successions at the Ordovician–Silurian transition, South China: possible sedimentary responses to the accretion of Cathaysia to the Yangtze Block and its implications for the evolution of Gondwana. Gondwana Res. 15, 111–130.

Them, T.R., Jagoe, C.H., Caruthers, A.H., Gill, B.C., Grasby, S.E., Gröcke, D.R., Yin, R., Owens, J.D., 2019. Terrestrial sources as the primary delivery mechanism of mercury to the oceans across the Toarcian Oceanic Anoxic Event (Early Jurassic). Earth Planet. Sci. Lett. 507, 62–72.

Thibodeau, A.M., Ritterbush, K., Yager, J.A., West, A.J., Ibarra, Y., Bottjer, D.J., Berelson, W.M., Bergquist, B.A., Corsetti, F.A., 2016. Mercury anomalies and the timing of biotic recovery following the end-Triassic mass extinction. Nat. Commun. 7, 11147.

Wolfenden, S., Charnock, J.M., Hilton, J., Livens, F.R., Vaughan, D.J., 2005. Sulfide species as a sink for mercury in lake sediments. Environ. Sci. Technol. 39, 6644–6648.

Yin, R., Feng, X., Hurley, J.P., Krabbenhoft, D.P., Lepak, R.F., Hu, R., Zhang, Q., Li, Z., Bi, X., 2016. Mercury isotopes as proxies to identify sources and environmental impacts of mercury in sphalerites. Sci. Rep. 6, 18686.

Zhang, T., Shen, Y., Zhan, R., Shen, S., Chen, X., 2009. Large perturbations of the carbon and sulfur cycle associated with the Late Ordovician mass extinction in South China. Geology 37, 299–302.

Zheng, W., Gilleaudeau, G.J., Kah, L.C., Anbar, A.D., 2018. Mercury isotope signatures record photic zone euxinia in the Mesoproterozoic ocean. Proc. Natl. Acad. Sci. USA 115, 10594–10599.

Zhou, L., Algeo, T.J., Shen, J., Hu, Z., Gong, H., Xie, S., Huang, J., Gao, S., 2015. Changes in marine productivity and redox conditions during the Late Ordovician Hirnantian glaciation. Palaeogeogr. Palaeoclimatol. Palaeoecol. 420, 223–234.

Zhu, W., Song, Y., Adediran, G.A., Jiang, T., Reis, A.T., Pereira, E., Skyllberg, U., Björn, E., 2018. Mercury transformations in resuspended contaminated sediment controlled by redox conditions, chemical speciation and sources of organic matter. Geochim. Cosmochim. Acta 220, 158–179.